Influence of a Conical Axial Injector on Hybrid Rocket Performance

C. Carmicino[*] and A. Russo Sorge[†]

University of Naples "Federico II," 80125 Napoli, Italy

This paper analyzes the results obtained from a series of static firings of a lab-scaled hybrid rocket in which gaseous oxygen was supplied into axial-symmetric polyethylene cylindrical grains through two different injector configurations: an axial conical subsonic nozzle and a radial injector. The axial injector is interesting because of its relatively easy design, the higher regression rates, and the noticeably stable motor operation. To exploit its qualities, not only the assessment of the regression rate but rather the entire behavior of the motor is required. For the investigated set of operating conditions, the instantaneous regression rates exhibit a time dependence caused by the impinging jet zone dynamics, while the average regression rates are higher and less mass flux dependent than those achieved with the radial injection motor and expected from the classical turbulent-boundary-layer diffusion-limited theory. A comparison to the data from the radial injector was further drawn in terms of combustion efficiency and fuel regression uniformity. Concerning combustion stability, some observations are made. The radial injector, at the same mass flux and pressure, produces lower regression rates, high pressure oscillations, and worse combustion efficiency, but more uniform fuel consumption.

Nomenclature

$\mathcal{A}$ = preexponential factor
A_e = nozzle exit area
A_t = nozzle throat area
B = blowing number
c_d = nozzle discharge coefficient
c_{ref} = speed of ultrasounds in reference conditions
c^* = characteristic exhaust velocity
c_0^* = theoretical characteristic exhaust velocity calculated at O/F
$\bar{c}^*$ = theoretical characteristic exhaust velocity calculated at $\overline{OF}$
D = space average port diameter
D_0 = port initial diameter
D_2 = average port final diameter
D_{2x} = local port final diameter
d = diameter
E_a = activation energy
F = motor thrust
G = mass flux
H_v = effective heat of vaporization
I_m = mixing index
L = grain length
L_c = prechamber length
L^* = chamber characteristic length
l = exponent of the Reynolds number in the mixing index definition
m = exponent of the geometrical ratio in the mixing index definition
$\dot{m}_f$ = fuel mass flow rate
$\dot{m}_{\mathrm{ox}}$ = oxidizer mass flow rate

$\dot{m}'$ = isentropic one-dimensional mass flow rate through the nozzle
N = number of data points in the port diameter profiles
n = exponent of mass flux
$\overline{OF}$ = spatially averaged oxidizer-to-fuel ratio
$\overline{OF}$ = mean value of spatially averaged oxidizer-to-fuel ratios
O/F = average oxidizer to average fuel mass ratio
p_a = ambient pressure
p_e = nozzle-exit pressure
$\mathcal{R}$ = gas constant
Re = Reynolds number
$\dot{r}$ = space average regression rate
$\dot{r}_x$ = local regression rate
s = fuel grain thickness
T_w = fuel surface temperature
t = time
V_e' = isentropic one-dimensional velocity at nozzle exit
x = axial abscissa
z = nondimensional axial abscissa (x/L)
α = nozzle divergence cone half-angle
ΔM_f = measured solid fuel mass loss
$\Delta M_f'$ = computed solid fuel mass loss
Δt = time step
Δt_o = ultrasounds time of flight
η = c^* efficiency, ratio between the actual and theoretical c_{th}^*
η_0 = c^* efficiency calculated at O/F
λ = momentum-thrust reduction coefficient
μ = gas viscosity
ρ_f = solid fuel density
σ = standard deviation of the local port final diameter

Subscripts

exp = experimental
j = injector exit section
max = maximum fuel consumption point
ox = oxidizer
st = stoichiometric (combustion products CO_2 and H_2O)
t = nozzle throat
th = theoretical

Superscript

— = time-average value

*Postdoctoral Appointee, Department of Space Science and Engineering "L. G. Napolitano," Piazzale Tecchio 80. Member AIAA.
†Associate Professor, Department of Space Science and Engineering "L. G. Napolitano," Piazzale Tecchio 80. Member AIAA.

Introduction

HYBRID rockets are propulsion systems in which one of the two propellants is stored in liquid phase (usually the oxidizer) and the other in solid phase. The oxidizer is injected into a port in the solid grain, where it reacts with the fuel vaporized as a result of the pyrolysis of solid grain subjected to heat-transfer from the flame zone. Oxidizer injection effects on the fuel regression rate are one of the most important aspects of hybrid combustor design even though they are often undervalued when dealing with classical hybrid motor configurations. Here by "classical configurations" we mean the engine arrangements in which a head-end injector is employed and an axial mean flow is established in the fuel port. The available literature presents some examples of oxidizer injection systems specifically designed to substantially modify the convective heat-transfer mechanism in order to raise the regression rate; for instance, a swirl injector, set up between the aft end of the grain and the nozzle inlet, generates a bidirectional vortex flowfield[1] such that, with the same propellant and oxidizer mass flux, the average regression rate is up to seven times larger.[2] This configuration was successfully studied in an effort to enhance the low burning rate of solid fuels, which requires a relatively large fuel surface area for a given thrust level. However, we will not refer to these unconventional configurations.

Injector and head-end design, in fact, can significantly affect the overall behavior of the motor in terms of such important characteristics as the thrust produced and its maintenance over time, the fuel consumption uniformity, the combustion efficiency, and the combustion stability. It is important to recognize that oxidizer injection can alter the regression rate throughout the entire grain and render inapplicable the ballistic calculations based on the classical boundary-layer model.

The solid fuel regression rate is the fundamental parameter needed for modeling the hybrid internal ballistics, but, although hybrids have been known since the 1930s (Ref. 3), a thorough knowledge of the regression process seems still somewhat lacking. Actually, for the sake of simplicity, in the classical hybrids, on the basis that, in the usual operating conditions, the combustion process is diffusion limited, the regression rate is often assumed to be only mass flux dependent according to the semi-empirical relationship $\dot{r} = aG_{ox}^n$, in which the preconstant a is considered linked to the propellant system and the exponent n is generally variable between 0.6 and 0.8, though values out of this range were also found.[4] In reality, provided that the diffusion-limited theory developed by Marxman and Gilbert[5] is applicable, no easy formulas, like those mentioned earlier, can be used to describe the phenomenon suitably. The regression-rate behavior depends strongly on the particular port size as well as grain length-to-diameter ratio and can change significantly with burning time. This makes it likely that both a and n would vary with the specific port geometry, the firing duration, and the mass flux itself. This regression-rate mass flux dimensional correlation is, then, definitely inappropriate for the purpose of scaling to motors having different dimensions and/or other propellant combinations. However, even considering the same propellant and characteristic dimensions, the application of this relation to other motors can lead to considerable disagreements between the expected and the measured regression rates, and one reason is certainly represented by oxidizer injection effects whereby the boundary layer can be disturbed or, in some cases, still inexistent.

Hence, there is a real need to study the injector influence on the combustor thermofluid dynamics to develop reliable tools for the prediction of regression rate under different flow conditions.

In an earlier paper[6] the authors showed that, if the oxidizer is fed into the fuel port by a conical axial nozzle, the recirculation region, established between the gaseous oxidizer jet boundary and the fuel grain's surface upstream of the impingement region, induces a convective heat flux to the fuel wall, which is higher and differently distributed when compared with the one in the turbulent flow through straight constant-cross-section pipes. Rather, the flowfield and the ensuing heat-transfer distribution in this condition are almost similar to those in a solid fuel ramjet having a sudden expansion of airflow. In fact, in both axial injector hybrid motor and solid fuel ramjet, three distinct flow regions exist[7] (see Fig. 1):
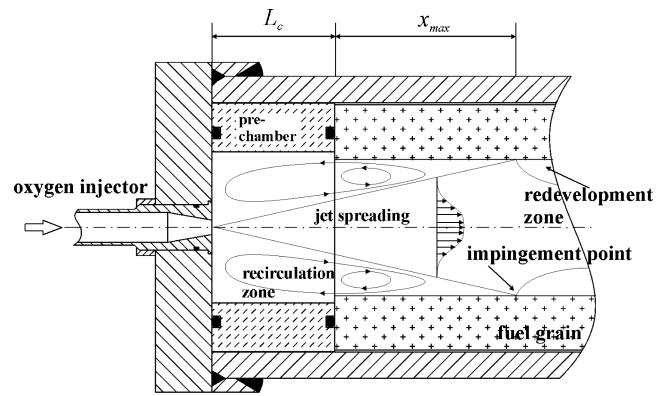
Fig. 1   Axial injection hybrid rocket with the main flow characteristics.

1) recirculation zone into which oxygen is transported from the jet core across the turbulent shear layer (Here, fuel provided from the wall is recirculated and reacts with oxygen near the head end of the grain; as pointed out by Shulte et al.,[8] the flame initiates along the shear layer); 2) impingement or reattachment region where the oxygen attacks the grain surface; and 3) the zone downstream of oxidizer impingement, where the turbulent boundary layer starts developing. Within this boundary layer a diffusion flame is, instead, formed.

This injection technique resulted in regression rates both increased (up to 2.5 times higher) and more or less unevenly distributed along the axis, depending on the ratio between the grain final diameter and the injector diameter. Furthermore, this flowfield leads to a lower dependence of regression rate on mass flux (smaller mass flux exponent, $n = 0.37$ as recalled later) and introduces a pure geometric effect, which is an explicit regression-rate dependence on the grain port diameter. Note that the oxidizer mass flux exponent derived in this study is very close to 0.4, which is the value theoretically predicted in the regime of kinetically controlled regression rate[9] ($\dot{r} \propto G^{0.4} p^{0.5}$). This singular issue can be possibly misleading because, then, a strong pressure effect could be inferred. However, if such an effect were present, this would be reasonably independent from the fluid dynamics in the combustor, that is, at the same mass flux and pressure, which means roughly at the same ratio between the characteristic diffusion time and reaction time; nearly the same regression-rate mass flux trend should be verified, independently of the injector used. But this is not the case, as we discuss in the forthcoming sections.

Besides the enhanced regression rate, the axial injector deserves careful attention because of its easy design and the remarkable feature that, as mentioned in Ref. 10, it is supposed to produce a stable combustion with no substantial pressure oscillations owing to the hot gas recirculation zone established within the combustion port. The number of valuable aspects just outlined can be of particular interest maybe for motor applications that do not need the highest thrusts. The work presented in the past paper[6] is here extended to analyze completely the performance of this motor in terms of combustion efficiency, fuel consumption regularity and, in a preliminary stage, combustion stability. To investigate carefully into this matter, a comparison to the experimental results achieved with a radial injector is further addressed. Another injector, indeed, was selected to generate different conditions for the oxidizer at the entrance of the fuel port with the aim of ascertaining the fluid dynamic impact on the regression rate. The experimental method used the ultrasound pulse-echo technique for the instantaneous regression-rate measurement in conjunction with the traditional time-space-averaged regression rates.

Moreover, a modified version of the usual integral techniques[4,11] for the reconstruction of ballistics data was developed for the special purpose of examining the variations of the combustion efficiency (measured as characteristic exhaust velocity efficiency) over time and with thermo-fluid-dynamic parameters. In the following sections, a description of this new efficiency assessment method is
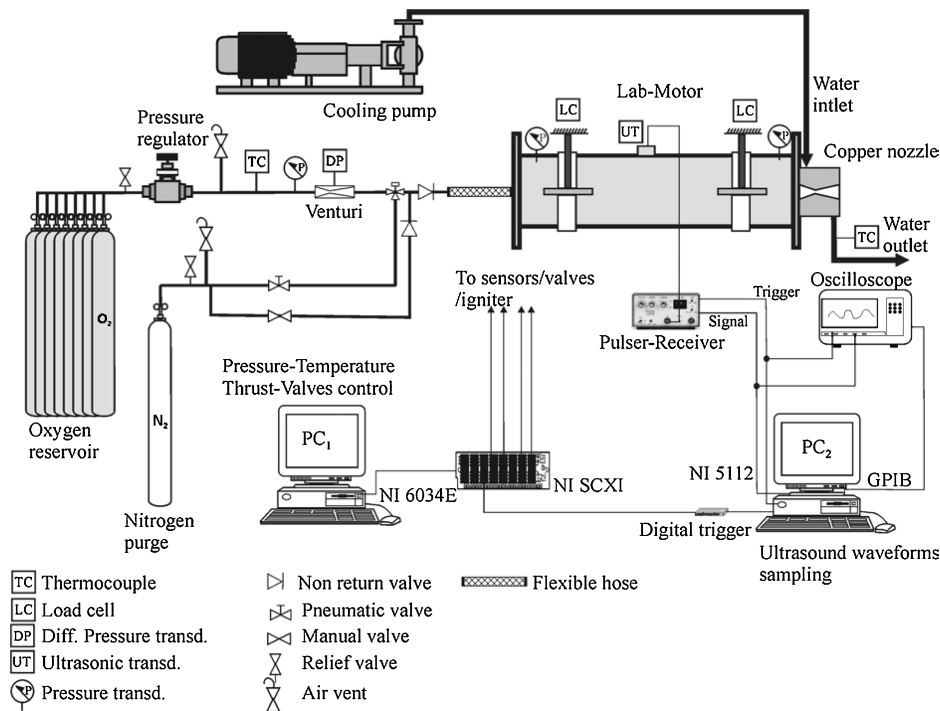
Fig. 2 Test facility.

provided. A comparison to the numerical results obtained with the diffusion-controlled regression-rate equation[5] is presented as well, to establish its applicability limit with respect to the particular injector configurations examined.

Experimental Techniques

Apparatus

A scheme of the test facility is depicted in Fig. 2. Gaseous oxygen is supplied by a reservoir of eight cylinders at mass flow rates up to 0.3 kg/s. The oxygen mass flow rate is calculated by measuring the gas temperature (with a copper-constantan thermocouple) and pressure (which allows to measure the gas density) at a section upstream from the throat of a nonchocked venturi tube and also measuring the differential pressure between this section and the throat itself.

Oxygen is axially injected into the combustion chamber through a converging nozzle whose exit diameter is 8 mm. The exit Mach number is at most 0.39. Nitrogen is purged into the chamber by a switch valve (oxygen or nitrogen) for the burnout and in case of an accident. By the way, it has to be said on behalf of hybrids, that no failure has ever occurred. The ignition was accomplished using a pyrotechnic cartridge electrically ignited 0.8 s before the oxygen injection.

The axisymmetric combustion chamber, 720 mm long and with a 133-mm inner case diameter, is suspended from the test bench by four load cells Tedea Huntlight model 1042 that have a good accuracy even with eccentric loading. (The error is about 0.005% of applied load per centimeter.) The motor thrust is computed as the sum of the loads measured by all of the cells.

High-density polyethylene fuel grains with one circular port, 560 mm or 533 mm long depending on the particular injector assembly, were tested. Four initial inner diameters, 16, 25, 50, and 75 mm, were chosen in order to explore a wide range of mass fluxes, grain length-to-diameter ratios and injector-to-grain port diameter ratios. Two chambers were placed before and after the grain: the first, made by Teflon®, to shift toward the fore end of the grain the strong recirculation region caused by the oxygen injection in an attempt to increase the overall regression rates; the second, made by stainless steel covered with thermal protections (manufactured by AVIO S.p.a.), to eventually improve the combustion efficiency.
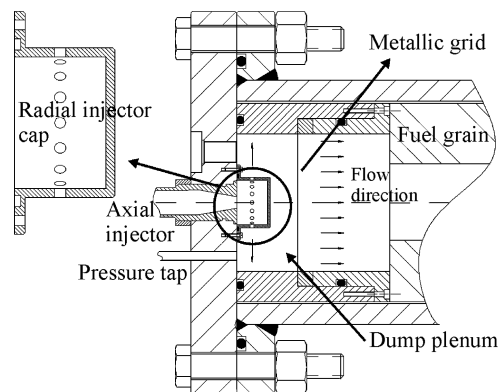
Fig. 3 Axial injector/radial injector and dump plenum at the head end of the motor.

The aft chamber is useful because it both promotes the gas mixing with further recirculation caused by the sudden expansion across the grain exit section and the aft chamber itself, and it raises the gas convection time with respect to the reaction time before gas is exhausted from the nozzle.

A second series of firing tests was carried out changing the injector configuration with a radial injector and a dump plenum (in stainless steel and slightly longer than the prechamber used with the axial injector setup). The radial injector cap, shown in Fig. 3, when assembled on the injection flange produces a high-speed radial flow of oxygen via 16 equally spaced 2.5-mm-diam orifices around the periphery of the cap.

This injection technique prevents the high recirculation that is instead yielded by the axial injector.[10] More precisely, in both configurations a large vortex ring should be produced,[10] but, for the radial injector, this vortex (clockwise rotating) should stand apart from the fuel grain forward face, whereas for the axial injector the vortex (counter clockwise rotating) can extend well into the combustion port. In addition, some tests were performed with a metallic grid placed in the dump plenum in order to eliminate the vortex produced and to provide a relatively uniform flow at the combustion port entry.

A water-cooled converging-diverging nozzle with 16-mm throat diameter, 2.44-area ratio, and a divergence cone half-angle $\alpha = 6$ deg, made of copper alloy, ensures long-duration firings with no throat erosion. Chamber pressure is measured by two capacitive transducers, Setra model 280E, set up in the prechamber and in the aft-mixing chamber. Because in all of the tests no significant pressure drop along the grain was yielded, only the prechamber pressure will be shown. The analog signals coming from thermocouples, pressure transducers, and load cells are sampled at 100 Hz, digitally converted, processed, and recorded on the hard disk by a National Instruments (NI) SCXI system interconnected with PC_1 in Fig. 2 via a NI 6034 E PCI device. With this equipment and utilizing a dedicated software developed in LabView 7, the motor is ignited, and the firing test is completely automated.

The instantaneous regression rate is measured by means of the ultrasound pulse-echo technique. One ultrasonic transducer, placed around the middle of the chamber (Fig. 2), is employed in order to acquire the local grain thickness variation over time. The ultrasonic transducer is a Panametrics Videoscan V114-SB of $\frac{3}{4}$ in nominal diameter and 1-MHz central frequency. The waves emitted by the transducer are electrically generated and, then, received and amplified by a pulser/receiver unit (Panametrics model 5072PR) with 100-Hz pulse repetition frequency. Two distinct techniques were applied to process the ultrasound waveforms as we present in the following section.

Ultrasound Signals Analysis

In the course of the test campaign on the axial injection hybrid motor, the ultrasound waveforms were acquired by an oscilloscope LeCroy LT344 and analyzed with an oscilloscope's proper function, which instantaneously calculates the time lapse between the trigger event (transmitted wave) and the first zero crossing point with positive slope of the solid–gas interface echo (Fig. 4) at 10 Hz (i.e., with nine-events hold-off).

This grain thickness sampling frequency is restricted by the oscilloscope performance, but, for quasi-steady regimes, it is believed a working value. The synchronization between the regression rate and other parameters measurements, that is, between the oscilloscope and PC_1 (see Fig. 2), was obtained using a GPIB. This method has the critical shortcomings that the ultrasound traces cannot be saved and further processed and that the regression-rate sampling rate cannot be increased. Recently, a new method has been developed for the ultrasound measurements: in this case the waveforms, emitted and acquired with a pulse repetition frequency at least equal to 100 Hz (10 times higher than the value limited by the oscilloscope), are sampled with 100-MHz rate by a NI 5112 PCI digitizer having 32-MB onboard memory and recorded by PC_1, while PC_2 is deputed to the acquisition of other experimental data and to the test control (see Fig. 2). A digital trigger is used for synchronizing both the acquisitions. Then, the ultrasounds signals are analyzed
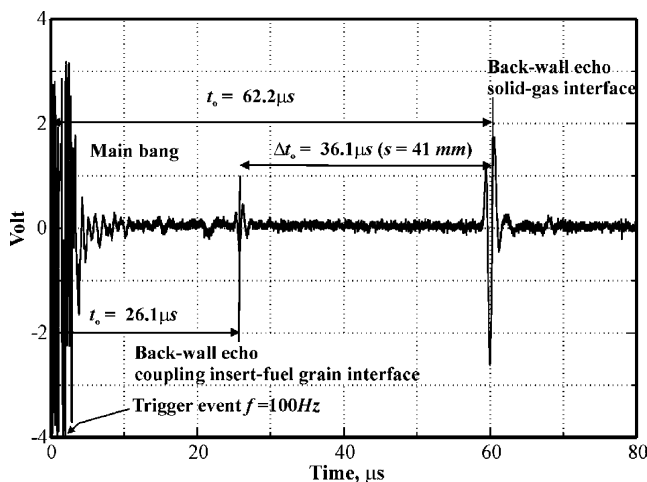
by a cross-correlation technique in order to compute the time delay between the coupling insert-external surface echo and the solid–gas interface echo (Fig. 4). This system is less prone to bias compared to the early used zero-crossing determination.[12] This method was applied only in the tests on the radial injection motor.

The grain thickness was calculated from the waves propagation time considering the wave speed in the fuel to be constant,[13,14] namely,

$$s = (\Delta t_o/2)c_{\text{ref}} \tag{1}$$

The thickness data were low-pass filtered, and then a central formula was applied to take the thickness derivative for the regression-rate calculation.

Data Reduction

The ranges of combustion chamber pressure and the oxygen mass flow rates covered in this study are 9.5–25 atm and 0.08–0.2 kg/s, respectively.

The fuel regression rates averaged over firing time and grain surface were determined with the classical endpoint technique,[6,11] using the information of initial port diameter, fuel mass loss, and burning time. The latter was measured as the difference between the inflection points identified on the diagram of chamber pressure vs time in the decrease and initial rise portions respectively. The test duration uncertainty consequent on this method is estimated to be at most ±9.5% (Ref. 6). This uncertainty, of course, affects all of the parameters involving the burning time, for example, the fuel mass flow rate, the regression rate, the c^* efficiency, and the Reynolds number.

The average mass flux was calculated dividing the average propellant mass flow rate (oxidizer mass plus fuel mass) by the average area of the port cross section evaluated at the mean port diameter. Note that, as suggested in Ref. 15, this averaging technique is the most accurate for estimating the mass flux. The average experimental characteristic exhaust velocity c_{exp}^* was estimated based on its definition, through the measured chamber pressure and total mass flow rate

$$c_{\text{exp}}^* = \bar{p} A_t \big/ \left(\bar{\dot{m}}_{\text{ox}} + \bar{\dot{m}}_f\right) \tag{2}$$

Finally, the average theoretical characteristic exhaust velocity c_0^* was computed at the average pressure and oxidizer-to-fuel-mixture ratio (O/F) (this was calculated taking the ratio between the average oxidizer mass and the average fuel mass) with the CEA chemical equilibrium code[16] assuming equilibrium upstream of the nozzle throat and frozen composition after this point in order to have possibly a better estimate.[17] The fuel vapor at the wall was supposed to be composed of the ethylene monomer at grain's surface temperature. The latter, because the regression rate is known experimentally, was estimated by means of an Arrhenius form for the regression rate as a function of the fuel surface temperature[6]

$$T_w = \frac{E_a/2R}{\ell_n(A/\dot{r})} \tag{3}$$

where the activation energy E_a and the preexponential factor A were taken from Ref. 18 and are equal to 4.78×10^6 mm/s and 60 kcal/mole, respectively. Note that the surface temperature predicted using these values is about 950 K, which is higher than one would expect from experimental observations, as also noted in Ref. 19. However, it has to be observed that the fuel surface temperature, in a variation range of 150 K, has just a little effect on the thermochemical parameters (e.g., the theoretical c^* and the blowing number, which will be considered later, have a change of about 0.4% varying the temperature from 800 to 950 K), and even a constant value could be used for our purposes.

In conjunction with the local regression rate measured with ultrasounds and the classical averaging technique, a method for the ballistic calculation of the spatially averaged regression rate, port diameter, and c^* efficiency, starting from the experimental chamber pressure, oxidizer mass flow rate and motor thrust, was developed.

Fig. 4   Typical ultrasound waveform.

Under quasi-steady operation, the motor thrust F can be expressed as follows (for an in-depth experimental and theoretical analysis see, for example, Ref. 20), it being assumed that the same static pressure exist at outlet in the actual and ideal conditions:

$$F = \dot{m}' V_e' c_d \lambda + (p_e - p_a) A_e \qquad (4)$$

where $\dot{m}'$ is the isentropic one-dimensional mass flow rate ejected through the nozzle at the effective chamber conditions (gas temperature and composition), V_e' is the velocity at the exit section of the nozzle for isentropic one-dimensional flow, c_d is a discharge coefficient that accounts for both non-one-dimensionality and non-isentropicity of the flow (which tend to reduce both the actual mass flow rate and exit velocity in comparison to the ideal case, so that c_d can be thought as the product of the mass flow efficiency factor and the velocity coefficient[21]), and $\lambda = (1 + \cos\alpha)/2 = 0.997$ is the momentum-thrust reduction factor[20–22] because of the nozzle's wall divergence. (Note that the effects of non-one-dimensionality and nonisentropicity are treated in isolation, but they could be merged resulting in a new scaled discharge coefficient.) Therefore, the so-defined nozzle discharge coefficient is, in fact, a momentum loss factor, which represents the ratio between the actual momentum thrust and the isentropic one-dimensional one developed by the nozzle exhausting the real-gas mixture at its real temperature. To separate the effect of nozzle characteristics from the influence of propellant combustion process (which likely leads to departures from the theoretical gas properties) on the momentum thrust, based on the c^* efficiency definition, one can write

$$F/pA_t = (V_e'/c_{th}^*)(c_d\lambda/\eta) + (p_e/p - p_a/p)(A_e/A_t) \qquad (5)$$

whence the efficiency can be derived:

$$\eta = \frac{\left(V_e'/c_{th}^*\right)c_d\lambda}{(F/pA_t) - [(p_e - p_a)/p](A_e/A_t)} \qquad (6)$$

From this equation, for a given value of c_d and a given oxidizer-to-fuel ratio, the efficiency can be calculated based on the nozzle geometry and the measured chamber pressure and motor thrust, through the values of V_e', c_{th}^*, and p_e output by the CEA code. Also in this case, the "infinite area combustor" model[16] with the nozzle throat as freezing point was used. With regard to the exit velocity V_e' and pressure p_e, a check was made on the nozzle operation to verify that the ratio p_a/p between the backpressure and the stagnation pressure was below the pressure ratio corresponding to a normal shock wave at the nozzle exit. If this condition were not satisfied, the exit velocity and, in turn, the thrust coefficient were corrected for the presence of a shock wave in the nozzle diverging section following the one-dimensional inviscid theory.[23] However, this condition was met only in few tests during the startup. Thus, within the framework of our model, η can be computed once the oxidizer-to-fuel mixture ratio OF has been determined. This is calculated, at each time step, by solving the equation of mass balance in which the density time derivative was neglected:

$$\eta[(1 + OF)/OF] - pA_t/\dot{m}_{ox}c_{th}^* = 0 \qquad (7)$$

where, in view of the preceding analysis, not only the theoretical exhaust velocity depends upon OF but also the efficiency η given by Eq. (6). All of the terms in this relationship have to be considered as functions of time. For the solution of Eqs. (6) and (7), the iterative execution of the CEA program is needed, which, in turn, requires the fuel temperature; the latter was calculated with Eq. (3) using the value of the OF at the preceding time step. Note that this is acceptable because, as a result of the large activation energy, a very large variation in the regression rate can be achieved with a relatively small temperature adjustment.

Once the spatially averaged OF_i at the time step $t = t_i$ is known, the fuel mass flow rate, the spatially averaged regression rate, and the new port diameter are calculated as follows:

$$\dot{m}_{f_i} = \dot{m}_{ox_i}/OF_i \qquad (8)$$

$$\dot{r}_i = \dot{m}_{f_i}/(\rho_f \pi D_i L) \qquad (9)$$

$$D_{i+1} = D_i + 2\dot{r}_i \Delta t \qquad (10)$$

in which the used time step is related to the sample rate, that is, $\Delta t = 10$ ms, and it is believed small enough to permit lagging the regression rate behind the port diameter with negligible error. Iterating this procedure until extinguishment, the total fuel mass consumed ΔM_f is computed as the integral of fuel mass flow rate over the burning time. This term, in the present scheme, actually, is a function of the discharge coefficient c_d, which is the unknown of the problem. The latter is found imposing that the fuel mass burned is equal to the measured one ΔM_f, that is, solving the following equation for c_d:

$$\Delta M_f'(c_d) - \Delta M_f = 0 \qquad (11)$$

The ballistic data reconstruction just described was carried out by means of a FORTRAN 90 numerical code; the choice was mostly dictated by the necessity of using a self-modified version of the CEA code. Pressure, oxygen mass flow rate, and thrust were filtered by running averages with 11-points period (0.1 s) when no large pressure oscillations were present; otherwise, a 101-points period (1 s) was used.

The solution of Eq. (7) was reached with the stopping criterion of 10^{-5} on the absolute value of the function, whereas Eq. (11) was solved with 1% accuracy on the fuel mass burned, that is, with a mass loss difference less than 10^{-2} kg. The algorithm used was a combination of linear interpolation, inverse quadratic interpolation, and bisection.[24] For both equations four to five iterations were necessary. For an indirect check on the model, the values of the converged discharge coefficient obtained are shown in Fig. 5 vs the nozzle throat Reynolds number, $Re_t = 4\dot{m}/(\pi d_t \mu_t)$. The latter, in effect, is known to be the most influential parameter in determining the discharge coefficient.[25]

Despite the dispersion of the data, it seems clear that c_d increases with the Reynolds number as expected, which, thus, can confirm the correctness of the adopted procedure. Note that the c_d's four values below 0.9 are all relative to the radial injector tests. As discussed subsequently, these motor tests were affected by large pressure oscillations for which c_d lower in value than the same at steady operating conditions is plausible. Moreover, c_d depends on the specific heat ratio, Prandtl number,[25] and on the wall heat flux (which all differ from test to test) as well, which should influence the data scatter.

In summary, this method has the advantage over the existing ballistic techniques to provide a direct measure of the efficiency and to allow for its variation during the rocket operation. This was possible collecting the additional information of motor thrust and making the nozzle discharge coefficient the unknown to be determined through the fuel total mass burned.

Finally, concerning the fuel consumption, the profiles of the post-firing port diameter were obtained by measuring the grain thickness at four circumferential locations with 45-deg shift and averaging over the results.
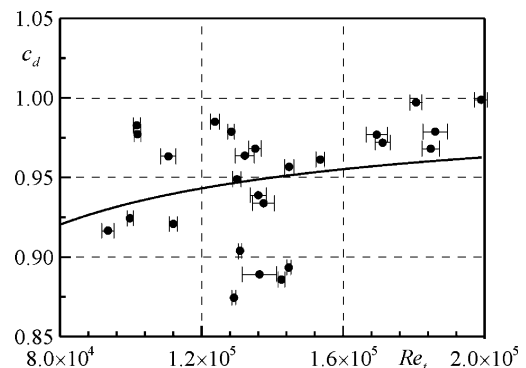
Fig. 5   Discharge coefficient as a function of the nozzle throat Reynolds number.

Table 1 Test table

Test	D_0, mm	$\dot{m}_{ox}$, kg/s	p, atm	$\bar{G}_{ox}$, kg/m²s	O/F	$\bar{\dot{r}}$, mm/s	c^*_{exp}, m/s	η_0	c_d	$\bar{\eta}$
				Axial injector						
1-A	25	0.14	15.63	99.69	2.74	0.69	1711.8	0.922	0.940	0.930
2-A	50	0.13	16.85	27.68	2.05	0.47	1843.5	0.952	0.958	0.988
3-A	16	0.12	17.31	63.87	2.50	0.58	2028.3	1.075	0.980	1.091
4-A	16	0.13	15.64	87.14	2.70	0.64	1795.7	0.965	0.950	0.972
5-A	16	0.12	15.46	92.43	2.76	0.63	1891.9	1.021	0.986	1.022
6-A	25	0.21	25.00	84.80	2.95	0.72	1814.2	0.984	1.000	0.999
7-A	25	0.16	18.96	66.60	2.83	0.59	1805.2	0.976	0.962	0.970
8-A	50	0.19	22.69	47.79	2.96	0.51	1828.2	0.994	0.998	0.990
9-A	75	0.18	22.61	28.41	2.50	0.47	1820.6	0.962	0.969	0.970
10-A	25	0.18	20.25	126.00	3.02	0.82	1747.9	0.955	0.978	0.986
11-A	50	0.17	20.78	47.45	2.73	0.55	1792.9	0.962	0.973	0.970
12-A	75	0.11	13.80	20.31	1.78	0.42	1690.8	0.869	0.890	0.914
13-A	50	0.08	10.09	28.19	2.05	0.38	1730.6	0.900	0.918	0.926
14-A	70	0.12	15.57	20.95	2.08	0.40	1816.2	0.941	0.969	0.964
15-A	75	0.11	15.12	20.12	1.90	0.41	1794.3	0.923	0.935	0.932
16-A	75	0.11	15.48	19.93	2.00	0.39	1871.8	0.967	0.965	0.992
17-A	50	0.10	12.20	34.13	2.19	0.44	1758.4	0.919	0.964	0.942
18-A	16	0.10	11.78	78.07	2.64	0.55	1740.8	0.936	0.978	0.956
19-A	25	0.09	11.11	54.03	2.37	0.50	1682.7	0.890	0.984	0.919
20-A	54	0.10	11.96	23.00	2.06	0.38	1701.9	0.884	0.922	0.892
21-A	50	0.08	9.57	18.77	1.76	0.35	1640.6	0.846	0.926	0.858
				Radial injector						
1-R	50	0.21	18.51	79.51	4.31	0.52	1456.1	0.853	0.980	0.860
2-R	67	0.16	13.52	38.02	5.91	0.23	1434.3	0.898	0.887	0.902
3-R	50	0.16	14.12	48.74	5.53	0.28	1455.6	0.899	0.895	0.902
4-R	25	0.15	13.33	77.99	5.03	0.38	1516.8	0.920	0.905	0.921
5-R	50	0.15	12.10	47.31	5.76	0.25	1419.1	0.886	0.876	0.892
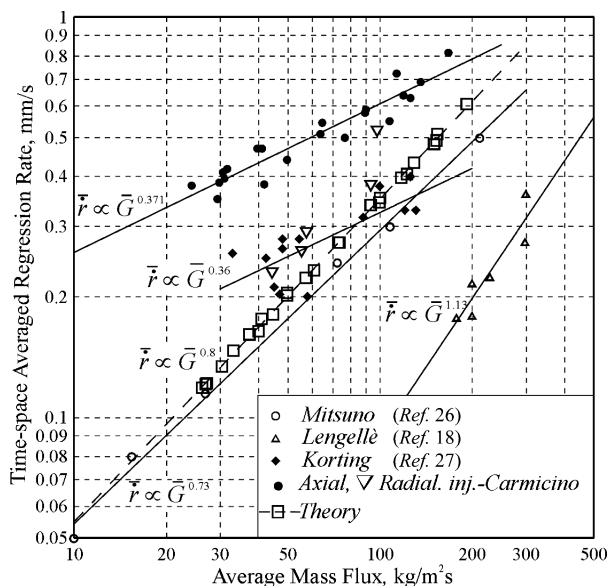
Fig. 6   Comparison of time- and space-averaged regression rates.

Experimental Findings and Discussion

Some relevant experimental and derived data for both axial and radial injection motor tests are given in Table 1.

The regression rates averaged over time and grain inner surface, for both the axial injector and the radial injector configurations, are reported in Fig. 6 as a function of the total mass flux with some data from the literature,[18,26,27] all of them being relative to experiments involving polyethylene fuel. In the same figure the theoretical points are also reported.

As argued in Ref. 6, the striking feature of this graph is that the regression rates achieved with the axial injector motor, at the same mass flux and chamber pressure, display greater magnitude and lower mass flux dependence compared to the data from the literature. According to Fig. 6, this distinct behavior, typical of the

axial injector motor, is further confirmed by the regression rates obtained with the radial injector motor. We recall here, for clarity, that this higher regression and weaker influence of mass flux are both consequences of the fact that the heat transfer is mainly governed by the impingement of the gaseous jet on the grain's surface, as also demonstrated by the concave port diameter profiles shown in Ref. 6. The fuel consumption, indeed, attained a maximum in the region of impingement whenever this was present in dependence on the injector-diameter-to-port-diameter ratio. The increase in the regression rate owing to the jet impingement is strongly accentuated as the mass flux decreases. An analogous trend for the convective heat-transfer coefficient relative to the one for a fully developed flow was noted by Krall and Sparrow.[28] At low mass fluxes $G \sim 30$ kg/m²s, the regression rate is 2.5 times higher and, by extrapolating, on achieving still lower mass fluxes, $G \sim 15$ kg/m²s, 3.8-times increase can be deduced. Whereas at $G \sim 200$ kg/m²s, the regression rate increase drops down to about 1.6 times. This aspect can represent a focal point for the design of small hybrid rocket engines.

Actually, two different regimes can be distinguished during the operation of the axial injection hybrid engine:

1) When the port diameter is sufficiently smaller than the jet diameter at the fuel port entry (which, of course, is determined by the ratio L_c/d_j), the flowfield is similar to a turbulent developing flow through pipes.

2) When the port diameter is larger than the jet diameter, the oxidizer jet penetrates into the fuel port impinging on the grain's surface farther downstream as the fuel is consumed.

In this condition a wide recirculation region is established upstream of the impingement section. Hence, when starting from a small port diameter, for long firing the motor operates in both these regimes, and the local regression rate, ultrasonically measured, well registered this transition showing an increase when the oxidizer jet passed under the ultrasonic transducer location.[6] On the other hand, when relatively uniform conditions at the fuel port inlet are realized, for instance, with the radial injector, this behavior vanishes. The overall effect stemming from the interaction between the fuel port enlargement and the oxidizer jet dynamics is that the fuel production increases during the run. In Fig. 7 the spatially averaged oxidizer-to-fuel ratio, computed following the procedure described
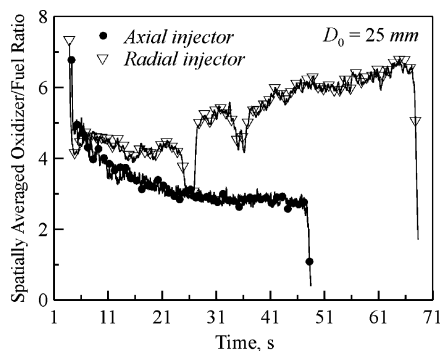
Fig. 7 Oxidizer-to-fuel-mixture ratio ballistically calculated.

Fig. 8 Blowing number and regression-rate percent error in a test.

earlier, is represented vs time for similar test conditions (oxidizer mass flow rate and initial port diameter) for both the axial and radial injection motors.

The different behaviors are markedly evident: OF for the radial injector increases while for the axial injector it decreases demonstrating that, for constant oxidizer flow rate, the fuel mass flow rate increases. This can be explained numerically considering that the regression rate, in this situation, varies approximately as a power of the mass flux with the exponent $n = 0.37$ (see Fig. 6). In fact, the fuel mass flow rate can be expressed as

$$\dot{m}_f = \rho_f \pi D \dot{r} L \propto \dot{m}_{ox}^{0.37} D^{0.26} \qquad (12)$$

which implies an increasing fuel mass flow when the grain port opens up. Incidentally, note that the unexpected quick rise of the fuel flow rate at the end of the test is caused by the model that fails to capture the transients, it being based on the steady mass balance of Eq. (7).

Theoretical Comparison

Proceeding with the investigation into the regression rate, in order to gain extra insight, it is useful to compare the regression rate expected from the classical turbulent boundary-layer regression-rate model[5] with that measured in this study.

Starting from the regression-rate equation developed by Marxman and Gilbert,[5] an expression for the spatially averaged regression rate along the port axis can be found (see appendix):

$$\rho_f \dot{r} = K G_{ox} \{1.25 + 2.5 K (L/D)[1 + K (L/D)]\} \qquad (13)$$

where the nondimensional parameter K is a function, in particular, of the blowing factor B. In this relationship, the regression rate appears as an explicit function of the oxidizer mass flow rate and port diameter (through the oxidizer mass flux), though it is an implicit function of the blowing number. In fact, the blowing number can be regarded as a thermodynamic factor,[5] which depends on the actual oxidizer-to-fuel ratio and pressure. Hence, Eq. (13) has to be considered strictly as an implicit function of OF. After rearranging the terms to show OF explicitly, Eq. (13) yields

$$\{1.25 + 2.5 K (L/D)[1 + K (L/D)]\} 4 K (L/D) OF = 1 \qquad (14)$$

The blowing parameter B was determined using the relationship derived by Marxman et al.[29]

$$B = \frac{1 + (1 + OF)\Delta h / H_v}{OF} \qquad (15)$$

where Δh is the enthalpy difference between the flame and the wall, which was calculated under chemical equilibrium conditions with the CEA[16] code, and H_v is the effective heat of vaporization estimated as reported in Ref. 30.

Equation (14) was numerically solved[24] at each time step, provided the actual pressure and oxidizer mass flow rate. Once OF was found, the regression rate was calculated with Eqs. (8) and (9). Note that by considering the blowing number constant throughout the burning, that is, independent of the mixture ratio, the regression rate
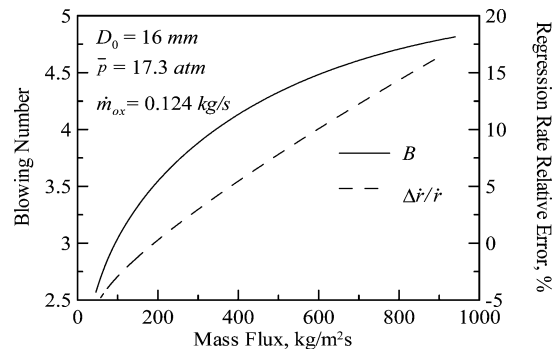
would be affected by a nonnegligible error. In Fig. 8 the blowing number and the relative regression-rate error consequent on assuming the blowing number constant, exactly equal to its average value over the test, and, thus, on using Eq. (13) for the regression-rate explicit calculation, are reported as functions of the total mass flux for a particular test condition. Note that, because the regression rates are different, also the respective mass fluxes are slightly different. This test was chosen because the oxidizer-to-fuel ratio nearly varied from 2 to 6 resulting in a variation of the blowing number from 4.8 to 2.6, which is about 60%. The latter leads to a relative error in the regression-rate calculation that varies between 16 and −5.5%. Of course, this error is much lower than the blowing number relative variation because B appears in the regression-rate equation as a power with the exponent equal to 0.32 (see appendix).

Interestingly, even making an error on the regression rate, the final port diameter is almost exactly predicted as can be deduced from the fact that the mass fluxes are practically coincident at the end of the test ($G \sim 46$ kg/m^{2}s in Fig. 8). The reason is twofold: first, the calculation was performed by precisely taking the blowing number as its average value, and, second, the little variation of $B^{0.32}$.

Following this procedure, the theoretical curve in Fig. 6 was plotted by best fitting the theoretical points derived at the experimental conditions (i.e., grain geometry, pressure, oxidizer mass flow rate, and total burning time) relative to the tests on both the axial and radial injection motors. Note that the average regression rate and the average mass flux of the theoretical points were determined according to the experimental data-reduction approach.

The theoretical regression rates and the radial-injection-motor regression rates are in good agreement except for the point at $G \sim 100$ kg/m^{2}s (Fig. 6), which represents a noticeably higher regression rate (about 0.5 mm/s). In this test high-pressure oscillations were present as we see later, thus affecting the regression rate. However, the faster fuel regression achieved with the axial injector is certainly validated by the theory.

Figure 9 shows a comparison between the regression rate measured by the ultrasound pulse-echo technique, the one spatially averaged computed with the ballistic procedure, and, finally, the one spatially averaged expected from the theory, for the axial injection motor having two different port initial diameters.

The theoretically computed regression rates in both cases (Figs. 9a and 9b) are lower than the measured ones. In fact, except for the initial instants ($t < 10$ s) in Fig. 9a when the theoretical regression rate is larger, it is always lower and even more decreasing over time as a result of the higher dependence upon the mass flux, which, obviously, decreases as the fuel is consumed. This difference displayed at the beginning of the test by grains with distinct initial port size might be caused by the transition from the regime, where the jet is still confined upstream from the port entry to a jet-dominated regime such that the recirculation and subsequent impingement occupy a wide portion of the fuel surface.

This could be argued also by observing the local regression rate trend, which, as indicated in Ref. 6, decreases until the jet impinges on the surface at the ultrasonic location. According to Fig. 9b, the average regression rate for this port size remains practically constant throughout the firing while the local regression
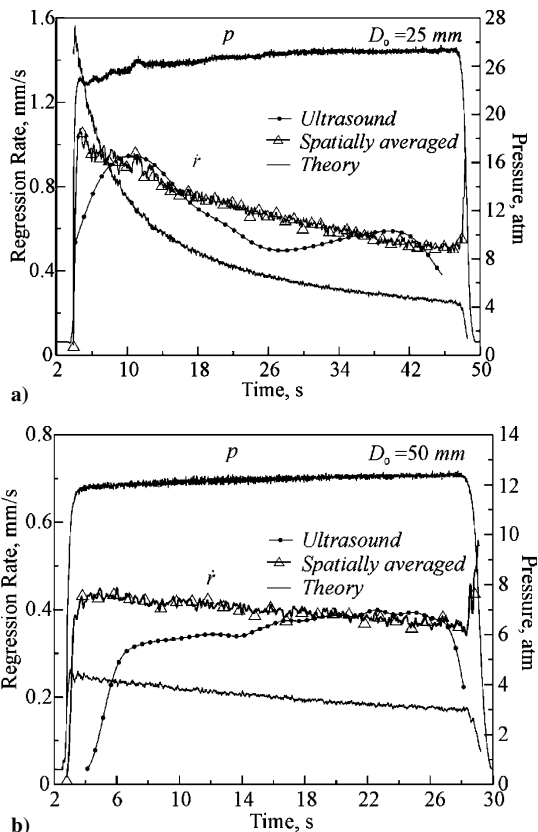
Fig. 9 Comparison between the regression rates in the axial injection motor.
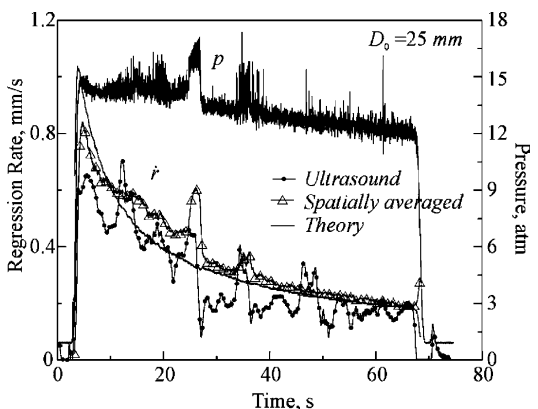
Fig. 10 Comparison between the regression rates in the radial injection motor.

rate slightly increases because, in this condition, the oxidizer jet tends to approach the transducer location slowly (see Ref. 6 again). A definite proof of the fundamental difference in the regression rates ensuing from different oxidizer conditions at the port entry is provided by Fig. 10. In this figure an analogous comparison between the regression rates is drawn for a typical test with the radial injection motor.

One can see that, at the same port initial diameter of Fig. 9a, there is a fairly good agreement between the regression rates. This issue, on one hand, demonstrates that, in this configuration, because the local regression rate follows the averaged spatially one the fuel consumption has to be almost uniform down the port; on the other hand, it shows that the theory surprisingly predicts the regression rate without adjusting any parameters. Precisely, the theoretical regression rate is slightly lower, as also shown by average data in Fig. 6, and this is can be caused by pressure oscillations. In fact, as expected from the literature,[10] the radial injection motor produced

unstable combustion characterized by large-amplitude pressure oscillations on the order of 5 atm, which are accompanied by enhanced fuel regression rates as demonstrated by the peaks roughly corresponding to the high-pressure oscillations onset (Fig. 10). This regression-rate sharp increase occurring during pressure oscillation periods has been also documented by Dijkstra et al.[31] Note that the oscillatory behavior of the local regression rate is captured by the ultrasound measurement technique. The latter was modified, in the radial injection test campaign, as outlined in the "Ultrasound Signal Analysis" section, in order to get higher sampling rate and better accuracy. The difference between the time resolution of the local regression rates shown in Figs. 9 and 10 is evident.

Finally, a comparison between the combustion stability characteristics of the axial and radial injection motors can be advanced at first glance. In reference to Figs. 9 and 10, the different chamber pressure behaviors of the motors are apparent. Apart from the mean trends that differ because for the axial injector motor pressure increases while for the radial injector one it, instead, decreases (as a consequence of the different regression rate behavior), the chamber pressure is really smooth in the motor with the axial injector, maybe for the stabilizing effect due to the recirculation zone within the fuel port.[10]

c^* Efficiency

As already cited, the c^* efficiency was measured in the course of the present experimental work. A factor enhancing the accuracy of the results is the absence of nozzle throat erosion for which the c^* measurement uncertainty is basically caused by the fuel mass flow rate evaluation that is associated with the firing time. The maximum uncertainty is estimated to be $\pm 3.5\%$. The major improvement offered by the data-reconstruction technique presented in the section "Data Reduction" is that it allows us to investigate into the combustion efficiency variation during the run. To validate the exactness of the predicted efficiencies, a comparison between the average efficiency over the steady state of each test $\bar{\eta}$ and the efficiency η_0

$$\eta_0 = c^*_{\exp}/c^*_0 \quad (16)$$

computed at the average pressure and at the average-oxidizer-mass-to-average-fuel-mass ratio was addressed. The result is shown in Fig. 11.

The average efficiencies ballistically calculated are very close to those evaluated at the average test parameters, as demonstrated by the amplitude of the relative difference band. More specifically, the ballistically calculated values show a bias being, in almost all of the cases, higher than the other efficiencies. The explanation can be found looking at the theoretical c^*_{th} plotted as a function of the mixture ratio in Fig. 12. In this calculation pressure and fuel surface temperature were chosen as the arithmetic means throughout all of the tests. The ratio between the average oxidizer mass and the average fuel mass O/F ranged over the tests between 1.7 and 5.8, but it was mostly near to 2.5. According to Fig. 12, all of these values are larger than the mixture ratio at which c^*_{th} attains its maximum (~ 1.6).

O/F can be related to the mixture ratio ballistically averaged over a single test $\overline{OF}$ and in particular for constant oxidizer mass
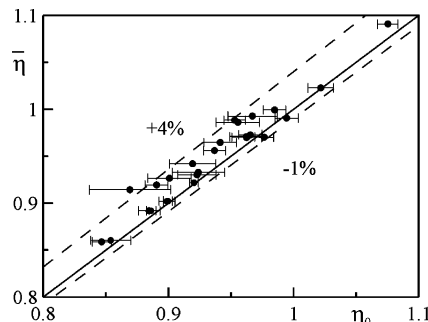
Fig. 11 The c^* efficiency comparison.
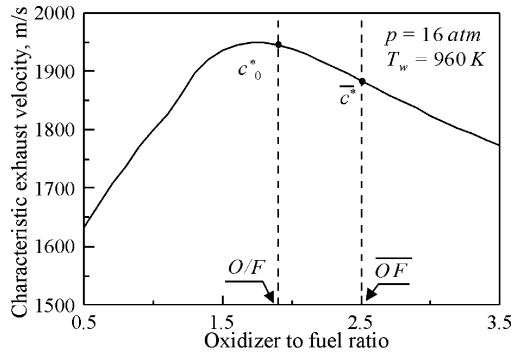
Fig. 12 The c_{th}^* as a function of the mixture ratio for typical values of pressure and fuel surface temperature over the tests.

Fig. 14 Average c^* efficiency vs O/F.
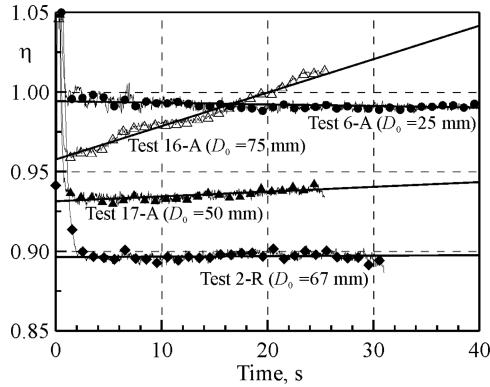
Fig. 13 Ballistically calculated c^* efficiency.

flow rate during the test the following relationship holds:

$$\overline{OF} = (O/F)\bar{m}_f \sum_i \left(\frac{1}{\dot{m}_{f_i}}\right) \qquad (17)$$

so that $\overline{OF}$ is always higher than O/F.

Thus, the corresponding theoretical characteristic velocities are such that $c_0^* > \overline{c^*}$, whereby the relative efficiencies, based on the same experimentally measured characteristic exhaust velocity, are in the inverse relation $\eta_0 < \bar{\eta}$.

In conclusion, this analysis gives a reason for the little discrepancy (at most 4%) between the efficiencies differently evaluated, and, at the same time, it constitutes a basis for the accuracy assessment of the efficiency given by Eq. (6).

The efficiency behavior over time is depicted in Fig. 13 both for the axial injection motor with several fuel port initial diameters (tests 6-A, 16-A, 17-A) and for one case relative to the radial injection motor with 67-mm grain initial diameter (test 2-R). Note that, during the first 2-s period, the efficiency is considerably higher than 1 and falls off steeply. This question has to be related to the hypothesis of steady regime in Eq. (4), which renders the model unable to predict the adjustments of the term F/pA_t in Eq. (6) resulting from the ignored gas inertia.

It is remarkable that, with regard to the hybrid engine with the axial injector, for $D_0 = 50$ and 75 mm, the efficiency increases, whereas it is approximately constant for the same motor with $D_0 = 25$ mm and for the radial configuration motor as well. Incidentally, in this context a comparison between the trends, rather than between the relative magnitudes, is believed appropriate because the latter might depend on parameters that vary from test to test.

It is well known that a limitation on the achievement of high efficiency in hybrid rockets is represented by the turbulent boundary-layer diffusion mechanism[32,33] from which strong propellant mixing suffers. Thus, an efficiency increase would be likely when the propellant mixing becomes more efficient, which occurs in the motor
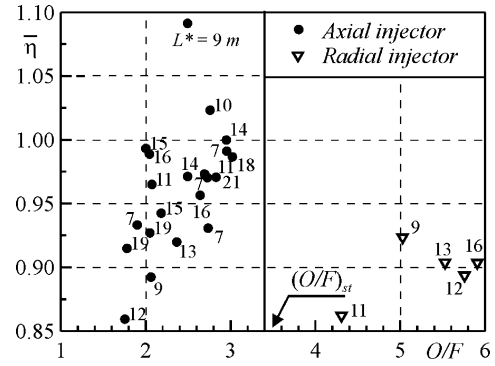
with the axial injector. The flow recirculation at the head end of the motor promotes the propellant mixing; therefore, it could be speculated that the growing efficiency (Fig. 13) is a consequence of the mixing region widening. The width of the recirculation region inside the fuel port, indeed, becomes larger as the port diameter is raised, and, stated that, in a single test, pressure and characteristic length L^* variations are very small, this subject should be responsible for the observed efficiency increase. On the other hand, this behavior was not experienced when $D_0 = 25$ mm (and $D_0 = 16$ mm but it is not shown here) and for the radial configuration motor.

To have a complete view of this topic, the average efficiency $\bar{\eta}$ was plotted as a function of the oxidizer-to-fuel ratio O/F in Fig. 14. The efficiency from the axial injection motor noticeably increases with O/F, displaying values mainly ranging between 90 and 100%, all of them being at fuel-rich mixture ratios, whereas the radial injection motor has lower efficiency close to 90% with oxidizer-rich mixture. The points in this graph are labeled with the relative L^* values (computed including the pre- and aft-chamber volumes), which indicate no explicit variation of efficiency with L^* itself. However, this increasing tendency is supposed to be correlated with propellant mixing rather than with stoichiometry. In fact, if a kinetics rather than mixing limitation were present, high efficiency on the oxidizer-rich side of stoichiometry would be expected.[34] Moreover, from the concentration measurements performed in a solid-fuel ramjet[8] the recirculation zone is expected to be fuel rich, accordingly to the axial-injector-motor results.

To the end of supporting this hypothesis, the product between a power of the jet Reynolds number and a power of the recirculation zone length to the port average diameter ratio $x_{max}/\bar{D}$ was identified as the index I_m of the mixing strength and its relative importance in the combustor cavity: $I_m = Re_j^l (x_{max}/\bar{D})^m$. Here, the abscissa of the point of maximum consumption on the fuel surface x_{max} (see Ref. 6) was assumed as the length of the recirculation area. The mixing index, defined in this way is, of course, just a roughly qualitative parameter. Figure 15 shows the c^* efficiency as a function of the mixing index just defined for the axial-injection-motor tests data. Obviously, the efficiencies derived from the radial injection configuration were not included in this analysis.

This figure is particularly interesting because, although the relative data spread, it seems to confirm our hypothesis: when the mixing index increases, the combustion efficiency increases too. Furthermore, Fig. 15 shows that O/F also increases with I_m, and this can be seen recalling the correlation of regression rate with mass flux and average diameter developed by the authors in Ref. 6:

$$\bar{r} \propto \bar{G}^{0.642} \bar{D}^{0.568} \qquad (18)$$

From this equation, with easy algebraic manipulations, one can show that, for the motor with the axial injector, O/F varies with the oxidizer mass flow rate and average port diameter as follows:

$$O/F \propto \bar{m}_{ox}^{0.358} \bar{D}^{-0.284} \propto Re_j^{0.358} (x_{max}/\bar{D})^{0.284} \qquad (19)$$

which predicts that O/F increases with the jet Reynolds number and decreasing average port diameter as the mixing index does. Note
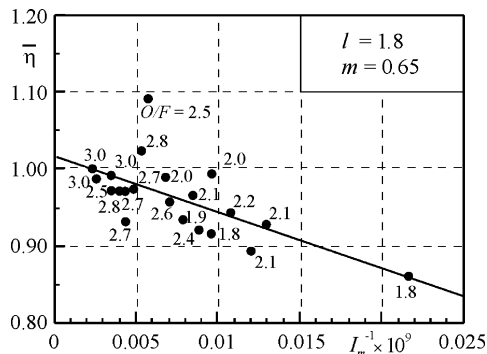
Fig. 15 Average c^* efficiency vs the inverse of the mixing index.
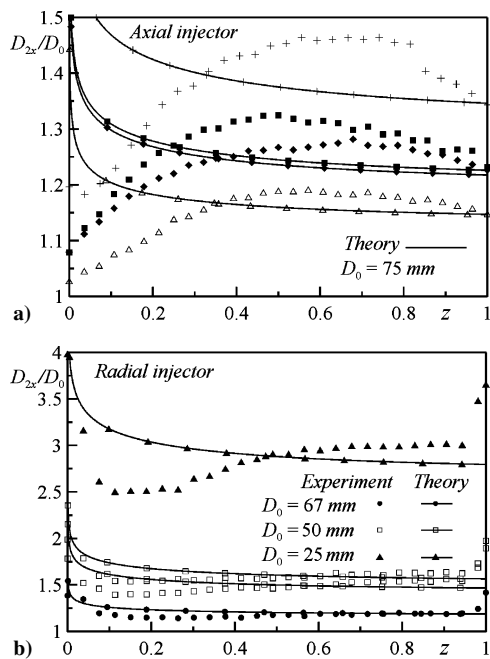
Fig. 16 Postfiring port diameter profiles.

that the last substitution follows from the fact that the ratio $x_{max}/\bar{D}$ varies linearly with the inverse of the port diameter.[6]

The importance of the mixing process in hybrid rockets is readily recognizable for the presence of a fuel-rich boundary layer near the fuel surface and an oxidizer-rich stream in the center of the combustor. Mixing between the fuel-rich and oxygen-rich regions was demonstrated to be necessary to achieve high combustion efficiency even in small engines.

Fuel Consumption Uniformity

A parameter that is very important to optimize is the fuel consumption regularity in order to reduce fuel slivers and inert mass. Unfortunately, when dealing with the axial injection hybrid motor, because of the jet impact on the grain's surface, for large ratios between the port diameter and the injector diameter, a concave consumption profile was yielded. As a result, the final port diameter concavity was severe when starting from large initial port diameters. This issue was not experienced using the radial injector as revealed by Fig. 16, in which the local afterburn port diameter D_{2x}, nondimensionalized by the initial port diameter, is plotted as a function of the nondimensional axial abscissa z. Figure 16a, for completeness, also shows the situation in the axial injection motor with the largest port initial diameter $D_0 = 75$ mm (Ref. 6); here all of the experimental curves, apart from the highest one that is relative to $\bar{m}_{ox} \cong 0.18$ kg/m²s, correspond to tests conducted with the same oxidizer mass flow rate ($\bar{m}_{ox} \cong 0.11$ kg/m²s) and with increasing burn time.

In Fig. 16, for the sake of comparison, the theoretical port diameter contours are plotted as well. The theoretical calculation was carried out with an integral technique[35] based on the spatial integration of the mass conservation equation along the fuel port (under the steady-state hypothesis) from which, starting from the initial conditions, the mass flux and local regression-rate distributions are derived. At the initial instant a uniform regression rate given by the solution of Eq. (14) is assumed; by integrating the regression rate over time, the port diameter distribution along the axis is calculated. The technique made use of a time-varying blowing number calculated at the spatially average oxidizer-to-fuel-mass ratio. The consistency between this calculation and the results achieved with Eq. (14) was checked. The theoretical port diameter contours were traced requiring that the port final average diameter was equal to the experimental one, that is, at the same amount of fuel consumed. This condition, of course, does not imply the same fuel mass flow rates because the experimental regression rate is faster.

The figure shows that the theoretical port diameter in all cases decreases monotonically from its maximum value at the grain leading edge with increasing distance. Note that at $z = 0$ the solution is not valid because the theory, based on the boundary-layer model, predicts infinite regression rate. The absolute discrepancy between the experimental and theoretical diameter contours is evident for the axial injection motor: the experimental profiles have a maximum point that moves downstream as the port enlarges while, from the theory, continuous decreasing diameters are expected.

In accordance with the profiles in Fig. 16b, the fuel consumption distributions in the radial injection motor are quite uniform, and, differently from the axial injection motor, they are in good agreement with the theory; moreover, the diameter contours are similar to the ones reported in Ref. 6 for $D_0 = 25, 16$ mm when the port-diameter-to-injector-diameter ratio is so low as to reduce the recirculation region width. Less uniform consumption and a displacement from the theoretically predicted profile in the port entry region are displayed by the afterburn port shape when the initial inner diameter is $D_0 = 25$ mm (Fig. 16b). This can be caused by a somewhat strong vena contracta effect because of the large sudden contraction the gas undergoes in this case as it moves from the dump plenum towards the combustion port.

The fuel consumption unevenness was quantified by taking the standard deviation σ of the grain local diameter after the burn:

$$\sigma = \sqrt{\frac{\sum_{i=1}^{N} \left(D_{2x_i} - D_2\right)^2}{N}}$$

To have an idea of the consumption uniformity relatively to other motor configurations, because, as far as the authors know, in the literature no experimental quantitative data are reported for a similar propellant combination (but also for different propellants they are very rare), a comparison between the theory and the experiments was addressed. Hence, σ was computed for the theoretical fuel port profiles derived as outlined earlier. For the calculation of the standard deviation, the narrow part of the curve near the port inlet (1 cm) was not included because, in this region, the regression rate tends to infinite. The results of this operation are shown in Fig. 17; here the ratio between the standard deviation and the port initial diameter is plotted as a function of the port average final-diameter-to-initial-diameter ratio.

In this way, all of the theoretical points nearly fall on the same curve. Note that, for a given initial diameter, the consumption unevenness, in terms of the standard deviation, increases with the average port diameter, whereas, for a given final diameter, the standard deviation is a decreasing function of the initial diameter.

The standard deviation of the experimental port diameter profiles is plotted in Fig. 18a. In this figure the data points relative to the axial injector are labeled with the percent fraction of fuel sliver M_{fr}, which is a parameter of immediate interest.

The latter is defined as the remaining mass of the fuel grain, whose maximum allowable diameter is $D_{2x\,max}$ (the maximum consumption to prevent case burn-through, i.e. the maximum diameter in the
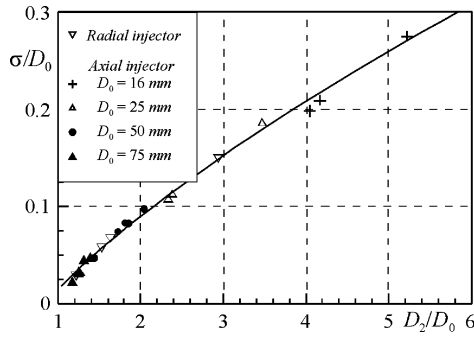
Fig. 17 Theoretical nondimensional standard deviation of port diameter profile.
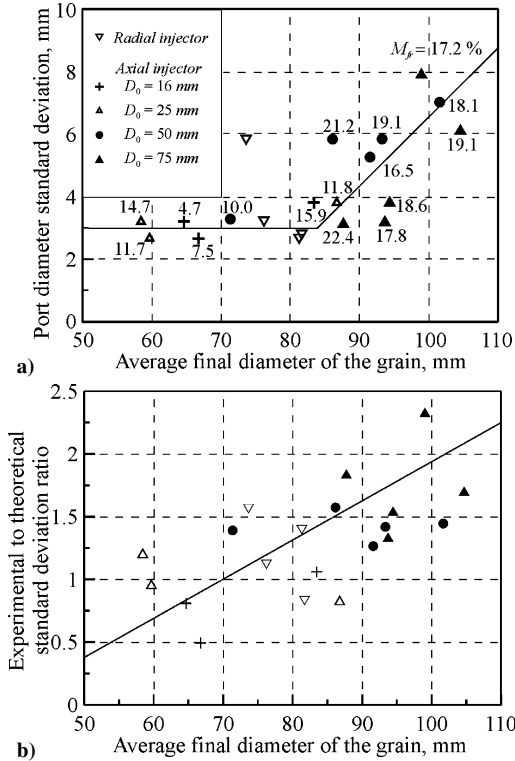
Fig. 18 Fuel consumption uniformity.

experimental profiles in Fig. 16a), to the initial mass of this grain, namely,

$$M_{fr} = \frac{1 - \int_0^1 (D_{2x}/D_{2x\,max})^2 \, dz}{1 - (D_0/D_{2x\,max})^2} \qquad (20)$$

One can observe that the fuel consumption of the axial injection motor, as long as the port final diameter remains sufficiently small compared to the injector diameter ($D_2 < 80$ mm), is fairly even, as demonstrated by the relatively low values of fuel mass sliver fractions (~10%) and of standard deviation (~3 mm). The latter, indeed, is equal to that achieved with the radial injector as mentioned earlier. For $D_2 > 80$ mm, the smooth final diameter profile tends to be concave, and the fuel consumption irregularity increases, whereby the standard deviation approaches 8 mm while the residual fuel mass fraction reaches values around 20%.

The same results are reported in Fig. 18b, where the ratio between the standard deviations of the experimental and theoretical diameter profiles is depicted vs the port average diameter. This graph suggests that, for the axial injection motor with $D_0 = 25$, 16 mm and for two cases relative to the radial injection motor with the smaller ratio D_2/D_0 (~1.5 or $D_2 \sim 80$ mm), the residual fuel mass is less than what would remain in a hypothetical motor in which the fuel

regression rate faithfully followed the theory. This could be caused by the unphysical excessive regression predicted in the entrance region of the grain. With increasing port final diameter the fuel consumption irregularity tends to be more pronounced relative to the theory. However, even in the worst case, when the final diameter gets the highest value of about 105 mm, the standard deviation of the axial-injection-motor-consumption profiles remains restricted to the double of that theoretically obtained.

Conclusions

This paper has to be considered as the second complementary part of the work presented in Ref. 6. In that work the authors analyzed the injection effects on the local and average regression rate in hybrid rocket engines, over a total mass flux range of about 20 to 200 kg/m²s in the combustion port. The selected axial injector configuration did allow the revealing of several detailed effects of fluid dynamic nature so far unreported in the competent literature. The ultrasound technique allowed the authors to collect interesting, and so far unavailable, local and instantaneous values of the regression rate. The average values, although similar to other experimental results obtained from polyethylene fuel grains, yet feature discrepancies with respect to the accepted trends. For the investigated set of operating conditions, the instantaneous regression rates exhibit a time and space dependence caused by the impinging jet zone dynamics while the average regression rates exhibit a weaker mass flux dependence and, very interestingly, higher values. The fuel regression is much faster as the mass flux decreases, which leads to attractive perspectives for small hybrid engines. This study was naturally completed by the examination of the performance achieved with this injector configuration, and, to accomplish this task, a comparison with another injector was drawn. Furthermore, a novel ballistic calculation was developed to measure the c^* efficiency variation during the firing. As it appeared from this paper, the combustion efficiency is at higher level than might be expected considering that a laboratory-scale test device is used. This feature is connected with the strong mixing of propellants promoted by the flow recirculation at the grain leading edge. Moreover, the combustion stability was fairly good. Though, a relatively fuel consumption irregularity was noted when the port diameter is large compared to the injector diameter. Of course, the hybrid designer needs to practice a tradeoff between the performance benefits deriving from this motor and the necessity to minimize the residual fuel.

Appendix: Average Regression Rate Equation

Following an approach similar to the one presented by Marxman et al.,[29] it is possible to formulate an analytical representation of the average regression rate down the fuel port.

The mass balance, under the steady-state regime and one-dimensional assumptions, requires that

$$dG = 4\rho_f \dot{r}_x (dx/D) \qquad (A1)$$

where the local regression rate $\dot{r}_x$ along the port axis is given by

$$\rho_f \dot{r}_x = 0.03G \, (Gx/\mu)^{-0.2} B^{0.32} \qquad (A2)$$

Note that the classical expression formulated by Marxman and Gilbert[5] was modified, as suggested by Altman and Humble,[35] to better estimate the blowing number influence.

Equation (A1) can be easily transformed, after the introduction of the regression-rate model stated in Eq. (A2), to yield

$$\frac{d(G/G_{ox})}{(G/G_{ox})^{0.8}} = 4\frac{L}{D} K z^{-0.2} \, dz$$

$$\text{with} \quad (G/G_{ox}) = 1 \quad \text{at} \quad z = 0 \qquad (A3)$$

where $K = 0.03(G_{ox}L/\mu)^{-0.2} B^{0.32}$ and $z = x/L$.

By integrating Eq. (A3), assuming constant port diameter, one obtains

$$(G/G_{ox})^{0.2} = 1 + (L/D)K z^{0.8} \qquad (A4)$$

Finally, by substituting Eq. (A4) into the regression-rate equation (A2), an explicit relationship between the regression rate and the oxidizer mass flux is obtained, namely,

$$\rho_f \dot{r}_x = K G_{ox} [1 + K(L/D) z^{0.8}]^4 z^{-0.2} \qquad (A5)$$

If $KL/D \ll 1$, as is often the case in practical systems ($KL/D \sim 5 \cdot 10^{-2}$), Eq. (A5) can be expanded in a power series neglecting all of the terms of order higher than the second, then

$$\rho_f \dot{r}_x \approx K G_{ox} \{1 + 4K(L/D) z^{0.8} + 6[K(L/D)]^2 z^{1.6}\} z^{-0.2} \quad (A6)$$

which now can be analytically integrated over z from 0 to 1 to yield Eq. (13).

Acknowledgment

References

[1]Vyas, A. B., Majdalani, J., and Chiaverini, M. J., "The Bi-Directional Vortex. Part 1: An Exact Inviscid Solution," AIAA Paper 2003-5052, July 2003.

[2]Knuth, W. H., Chiaverini, M. J., Sauer, J. A., and Gramer, D. J., "Solid-Fuel Regression Rate Behavior of Vortex Hybrid Rocket Engines," *Journal of Propulsion and Power*, Vol. 18, No. 3, 2002, pp. 600–609.

[3]Green, L., Jr., "Introductory Considerations on Hybrid Rocket Combustion," *Heterogeneous Combustion*, edited by H. G. Wolfhard, I. Glassman, and L. Green, Vol. 15, Progress in Astronautics and Aeronautics, Academic Press, New York, 1964, pp. 451–484.

[4]George, P., Krishnan, S., Varkey, P. M., Ravindran, M., and Ramachandran, L., "Fuel Regression Rate in Hydroxil-Terminated-Polybutadiene/Gaseous Oxygen Hybrid Rocket Motors," *Journal of Propulsion and Power*, Vol. 17, No. 1, 2001, pp. 35–42.

[5]Marxman, G. A., and Gilbert, M., "Turbulent Boundary Layer Combustion in the Hybrid Rocket," *Ninth International Symposium on Combustion*, Academic Press, New York, 1963, pp. 371–383.

[6]Carmicino, C., and Russo Sorge, A., "Role of Injection in Hybrid Rockets Regression Rate Behavior," *Journal of Propulsion and Power*, Vol. 21, No. 4, 2005, pp. 606–612.

[7]Karadimitris, A., Scott, C., II, Netzer, D. W., and Gany, A., "Regression and Combustion Characteristics of Boron Containing Fuels for Solid Fuel Ramjets," *Journal of Propulsion and Power*, Vol. 7, No. 3, 1991, pp. 341–345.

[8]Shulte, G., Pein, R., and Högl, A., "Temperature and Concentration Measurements in a Solid Fuel Ramjet Combustion Chamber," *Journal of Propulsion and Power*, Vol. 3, No. 2, 1987, pp. 114–120.

[9]Wooldridge, C. E., Marxman, G. A., and Kier, R. J., "Investigation of Combustion Instability in Hybrid Rockets," NASA Contract NAS 1-7310, 1969.

[10]Boardman, T. A., Brinton, D. H., Carpenter, R. L., and Zoladz, T. F., "An Experimental Investigation of Pressure Oscillations and Their Suppression in Subscale Hybrid Rocket Motors," AIAA Paper 95-2689, July 1995.

[11]Wernimont, E. J., and Heister, S. D., "Reconstruction Technique for Reducing Hybrid-Rocket Combustion Test Data," *Journal of Propulsion and Power*, Vol. 15, No. 1, 1999, pp. 128–136.

[12]Eriksson, H., Börjesson, P. O., Ödling, P., and Holmer, N. G., "A Robust Correlation Receiver for Distance Estimation," *IEEE Transactions on Ultrasonics, Ferroelectrics, and Frequency Control*, Vol. 41, No. 5, 1994, pp. 596–603.

[13]Traineau, J. C., and Kuentzmann, P., "Ultrasonic Measurements of Solid Propellant Burning Rates in Nozzleless Rocket Motors," *Journal of Propulsion and Power*, Vol. 2, No. 3, 1986, pp. 215–222.

[14]Carmicino, C., "Alcuni Aspetti Della Balistica Interna di un Endoreattore a Propellenti Ibridi e del Comportamento di Ugelli a Spina Troncata," Ph.D. Dissertation, Dept. of Space Science and Engineering "L. G. Napolitano" Univ. degli Studi di Napoli "Federico II," Italy, Nov. 2002.

[15]Karabeyoglu, A., Cantwell, J. B., and Zilliac, G., "Development of Scalable Space-Time Averaged Regression Rate Expressions for Hybrid Rockets," AIAA Paper 2005-3544, July 2005.

[16]Gordon, S., and McBride, B. J., "Computer Program of Complex Chemical Equilibrium Compositions and Applications," NASA Reference Publ. 1311, Oct. 1994.

[17]Furstenau, R., and Humble, R., "Thermochemistry," *Space Propulsion Analysis and Design*, edited by R. W. Humble, G. N., Henry, and W. J. Larson, 1st ed., McGraw-Hill, New York, 1995, Chap. 4.

[18]Lengellé, G., Fourest, B., Godon, J. C., and Guin, C., "Condensed Phase Behavior and Ablation Rate of Fuels for Hybrid Propulsion," AIAA Paper 93-2413, June 1993.

[19]Karabeyoglu, A., Cantwell, B. J., and Stevens, J., "Evaluation of Homologous Series of Normal-Alkanes as Hybrid Rocket Fuels," AIAA Paper 2005-3908, July 2005.

[20]Herbert, M. V., Martlew, D. L., and Pinker, R. A., "The Design-Point Performance of Model Internal-Expansion Propelling Nozzles with Area Ratios up to 4," Ministry of Technology, Aeronautical Research Reports and Memoranda No. 3477, London, 1963, pp. 25, 43.

[21]Zucrow, M. J., and Hoffman, J. D., *Gas Dynamics*, Vol. 1, Wiley, New York, 1976, Chap. 4.

[22]Sutton, G. P., and Biblarz, O., *Rocket Propulsion Elements*, 7th ed., Wiley, New York, 2001, Chap. 3.

[23]Hodge, B. K., and Koenig, K., *Compressible Fluid Dynamics*, Prentice–Hall, Upper Saddle River, NJ, 1995, Chap. 6.

[24]Brent, R. P., "An Algorithm with Guaranteed Convergence for Finding a Zero of a Function," *The Computer Journal*, Vol. 14, No. 4, 1971, pp. 422–425.

[25]Tang, S. P., and Fenn, J. B., "Experimental Determination of the Discharge Coefficients for Critical Flow Through an Axisymmetric Nozzle," *AIAA Journal*, Vol. 16, No. 1, 1978, pp. 41–46.

[26]Mitsuno, M., Kuwabara, T., Kosaka, K., and Shirota, K., "Experimental Study on Solid Fuel Ram Rocket," International Astronautical Federation, IAF80-F269, Sept. 1980.

[27]Korting, P. A. O. G., Schöyer, H. F. R, and Timnat, Y. M., "Advanced Hybrid Rocket Motor Experiments," *Acta Astronautica*, Vol. 15, No. 2, 1987, pp. 97–104.

[28]Krall, K. M., and Sparrow, E. M., "Turbulent Heat Transfer in the Separated, Reattached, and Redevelopment Regions of a Circular Tube," *Journal of Heat Transfer*, Vol. 8, Feb. 1966, pp. 131–136.

[29]Marxman, G. A., Wooldridge, C. E., and Muzzy, R. J., "Fundamentals of Hybrid Boundary Layer Combustion," AIAA Paper 63-505, Dec. 1963.

[30]Wilde, J. P. de, "The Heat of Gasification of Polyethylene and Polymethylmethacrilate," Prins Maurits Lab., Rept., 1988-C42, Solid Fuel Combustion Chamber Pub. No. 53, Delft Univ. of Technology, The Netherlands, Sept. 1988.

[31]Dijkstra, F., Korting, P. A. O. G., and van der Berg, R., "Ultrasonic Regression Rate Measurement in Solid fuel Ramjets," AIAA Paper 90-1963, July 1990.

[32]Netzer, D. W., "Hybrid Rocket Internal ballistics," Naval Postgraduate School, CPIA Publ. No. 222, Monterey, CA, Jan. 1972.

[33]Shadow, K. C., Cordes, H. F., and Chieze, D. J., "Experimental Studies of Combustion Process in a Tubular Combustor with Fuel Addition Along the Wall," *Combustion Science and Technology*, Vol. 19, May 1978, pp. 51–57.

[34]Strand, L. D., Jones, M. D., Ray, R. L., and Cohen, N. S., "Characterization of Hybrid Rocket Internal Heat Flux and HTPB Fuel Pyrolysis," AIAA Paper 94-2876, June 1994.

[35]Altman, D., and Humble, R., "Hybrid Rocket Propulsion Systems," *Space Propulsion Analysis and Design*, edited by R. W. Humble, G. N. Henry, and W. J. Larson, 1st ed., McGraw–Hill, New York, 1995, pp. 372–383.